



Immunizing sulfate-mediated deactivation over TiO₂ photocatalysts for gaseous benzene purification via self-adaptive deoxygenation of sulfate radicals

Wenqiang Qu¹, Penglu Wang¹, Xin Chen, Dongsong Zhang^{*}

International Joint Laboratory of Catalytic Chemistry, College of Sciences, Shanghai University, Shanghai 200444, China

ARTICLE INFO

Key words:

Environmental catalysis
Photocatalysis
Gaseous benzene purification
Sulfate
Deactivation mechanism

ABSTRACT

Interactions between complex components in atmosphere have always engendered an elusive and uncontrollable pathway for gaseous contaminants purification among environmental catalysis. Herein, an intriguing phenomenon was noticed in which trace exposure of sulfate, one of the most ubiquitous environmental matrices in atmosphere, will induce rapid deactivation of the benchmark TiO₂ photocatalysts for benzene purification. Fundamentally, the photogenerated sulfate radicals ($\bullet\text{SO}_4^-$) would selectively oxidize benzene into benzoquinone but subsequently become the nucleus of benzoquinone polymerization, resulting from the fact that insufficient reactive oxygen species (ROS) cannot interrupt the excess deoxygenation of $\bullet\text{SO}_4^-$ in time. Whereby, the curvature of Ti-O steps was tactfully manipulated to spontaneously create a ROS-enriched environment, which maintained the balance of the catalytic reaction cycle by recovering the reacted $\bullet\text{SO}_4^-$ back and detaching the benzoquinone analogues to proceed sequential reactions. This work offers an ingenious strategy to develop efficient photocatalysts for practical applications.

1. Introduction

The complicated interactions between atmospheric components are inevitable factors to be considered in the process of gaseous contaminants abatement, which always induces mutative elementary reactions and various by-products generation [1–3]. In the process of target contaminant remediation, other air pollutant components are easily involved into the degradation reaction in actual atmosphere and can be coupled to the reaction intermediates by strongly exoergic pathways, leading to the undesired side reactions [4,5]. Furthermore, the active sites of catalysts are commonly susceptible to the generated by-products, and then intertwined into a low-lying stable state, eventually leading to irreversible deactivation [6,7]. The interaction effects of the air pollutant components on the target degradation reaction and the catalyst deactivation mechanism have been in the spotlight, but still in obscure and require more insightful understanding [5,8,9].

Volatile organic compounds (VOCs), one of the most canonical atmospheric pollutants, are generally considered to be responsible for various environmental issues, such as PM_{2.5}, haze weather, etc. [10–13]. For now, the most prevalent and effective technique for VOCs

purification is aerobic catabolism for complete destruction, wherein photocatalysis provides an unparalleled and environmentally benign scenario on atmospheric contaminant remediation [14–16]. Following this mind, great strides have been taken on photocatalytic VOCs degradation, and tremendous wide-band-gap photocatalysts have been developed such as TiO₂, ZnO, SnO₂ and so on, as the wide-band-gap photocatalysts possess a lower valence-band position and thus delivering a strong photocatalytic oxidation potential [17–20]. However, most studies focused on developing new photocatalysts for various VOC degradation, and fewer researches considered the interaction between different air components. Recently, Li et al. [21] showed that the presence of NO was beneficial to the degradation of toluene, and a synergistic effect was revealed between NO and toluene for the inhibition of O₃ generation. Nevertheless, the interactions between air components during photocatalysis were still in its infancy [19, 22–26].

Indispensably in the actual air pollution remediation conditions, there are always plenty of other air pollutant components coexisting with VOCs, which involves kinds of ionic substances, such as sulfate, carbonate, ammonium, etc. [27–29]. These ionic substances may come from particulate matter or be generated by their correlating gaseous

^{*} Corresponding author.

E-mail address: dszhang@shu.edu.cn (D. Zhang).

¹ These authors contribute equally to this work.

contaminants [3,30,31]. Nevertheless, as matters stand, the impacts of ionic substances on the photocatalytic air purification have still existed as a hitherto unexplored field, but should be urgently figured out indeed for further applications of efficient catalysts [32,33].

In this contribution, the commercial TiO_2 catalyst was adopted for photocatalytic degradation of gaseous benzene, which was considered as the typical aromatic VOCs in atmosphere. Simultaneously, the effects of several common ionic substances in air (sulfate, carbonate, and ammonium salts) on the degradation reaction were studied by simply mixing these ionic substances with the TiO_2 photocatalyst. Perplexingly, the TiO_2 photocatalyst suffered from severe unalterable deactivation as soon as the sulfate was introduced into the benzene degradation process, while the other atmospheric ionic substances of carbonate and ammonium made no impact on this photocatalytic reaction. By means of spectroscopic analysis, the deactivation mechanism was corroborated where the photogenerated sulfate radicals ($\bullet\text{SO}_4^-$) exacerbated the aggregation of benzoquinone, sequentially interweaved into the aromatic molecule building blocks and contributed to the predicament of inferior performance. In order to combat deactivation, the TiO_2 photocatalyst was reconstructed in which the curvature of Ti-O configuration was tailored to create an enriched environment of reactive oxygen species (ROS) and the controlled ROS facilitated the decoupling process between $\bullet\text{SO}_4^-$ and the benzoquinone-analog monomer. Thereby, this self-adaptive deoxygenation of $\bullet\text{SO}_4^-$ guided by enriched ROS impeded the sulfate-mediated deactivation for photocatalytic purification of benzene.

2. Experimental section

2.1. Materials and chemicals

Sodium hydroxide (NaOH), hydrochloric acid (HCl), ammonium sulfate ($(\text{NH}_4)_2\text{SO}_4$) and ammonium carbonate ($(\text{NH}_4)_2\text{CO}_3$) were purchased from Sinopharm Chemical Reagent Co. Ltd. The commercial TiO_2 catalyst was purchased from the German Gussa company. All the reagents were employed without any further treatment.

2.2. Catalyst preparation

The reconstruction of TiO_2 was performed in accordance with the previous reports [34]. Briefly speaking, 1 g of TiO_2 was placed into the Teflon autoclave together with 70 mL 10 M NaOH solution, and laid up in 130 °C for 24 h. The precipitation was then washed with 0.1 M HCl aqueous solution, deionized water and ethanol, respectively. Eventually, the obtained product was dried at 80 °C and noted as H- TiO_2 . The obtained H- TiO_2 catalyst was then calcined at 400 °C for 3 h with a heating rate of 5 °C/min, and the powder was designated as R- TiO_2 .

The TiO_2 and R- TiO_2 catalysts were treated by impregnating ionic substances onto the surface of catalysts. More specifically, 1 g of TiO_2 (or R- TiO_2) was dispersed in 30 mL deionized water containing 20 mg of $(\text{NH}_4)_2\text{SO}_4$. After a process of rotary evaporation at 40 °C, the ionic substances were evenly deposited on the catalyst, spontaneously. The catalysts were denoted as $\text{TiO}_2\text{-SO}_4$ (or R- $\text{TiO}_2\text{-SO}_4$).

To verify the effects of Ti-O configuration curvature on the deactivation caused by sulfate deposition, the xylene-treated R- TiO_2 sample with the curved surface of R- TiO_2 filled was obtained. For preparation of the xylene-treated R- $\text{TiO}_2\text{-SO}_4$ sample, 1 g of R- TiO_2 was immersed in 30 mL xylene for 12 h to fill the channels with the xylene. After removing the excess xylene, the xylene-treated R- TiO_2 was then handled with $(\text{NH}_4)_2\text{SO}_4$ impregnation, which was the same with the treatment of R- $\text{TiO}_2\text{-SO}_4$.

2.3. Photocatalytic activity evaluation

The photocatalytic performance of benzene degradation was assessed in a continuous flow reactor, which we described previously

[18]. In detail, 80 mg photocatalysts were dispersed on the frosted quartz plate with deionized water and then dried at 60 °C. After the photocatalyst was placed into a 275 mL homemade reactor, the simulated polluted air was fed into the reactor with a flow rate of 36 mL/min under dark condition. The simulated polluted air was configured by the standard gas of 1000 ppm of benzene balanced with N_2 and high purity air (composed of 21% O_2 and 79% N_2 , without any other gas component).

When the benzene concentration in the reactor reached equilibrium, the degradation reaction was triggered by introducing the irradiation (Xenon Lamp, PLS-XE300, Perfectlight, Beijing). In order to simulate the humidity in the atmosphere, a certain amount of water vapor was added to the reaction gas by bubbling. The concentrations of benzene, H_2O and CO_2 were measured by a photoacoustic spectrometer analyzer (GASERA ONE, Beijing Duke Technology Co. Ltd.).

3. Results and discussion

3.1. Adsorption structure of SO_4^{2-}

The reconstruction of TiO_2 photocatalyst was manipulated in hydrothermal reaction and followed by calcination in air. After hydrothermal treatment, the XRD patterns in Fig. 1a showed that the commercial TiO_2 was reconstructed into hydrotitanate ($\text{H}_2\text{Ti}_8\text{O}_{17}$, denoted as H- TiO_2). Thereafter, with a thermal process, the $\text{H}_2\text{Ti}_8\text{O}_{17}$ evolved into anatase titanium dioxide, which was designated as R- TiO_2 . Simultaneously, Raman spectra (Fig. S1) suggested that the same Ti-O characteristic peaks were presented between R- TiO_2 and TiO_2 . Notably, the trace addition of the sulfate moiety did not influence the structure of catalysts in terms of the XRD pattern and Raman spectra. After the reconstruction, the R- TiO_2 macroscopically appeared as a nanotube structure (Fig. S2 and S3), which was consistent with our previous report [35]. The HRTEM image in Fig. 1b corroborated the hollow rod structure of R- TiO_2 , implying the obviously macroscopical bending structure configurations in R- TiO_2 .

The deposition of sulfate on the catalyst would influence the surface acid properties, which could be detected by pyridine infrared (Py-IR) spectra. After the sample was pretreated in vacuum at 200 °C for 30 min, the spectra were collected for the baseline. Then the temperature was reduced to 30 °C and the sample was exposed to gas pyridine. The pyridine molecules will specifically bind to the acid sites of the catalyst, such as Lewis acid sites (Ti sites) or Brønsted acid sites (H sites of hydroxyl). After the gaseous pyridine was adsorbed for 10 min, the sample was placed in a vacuum environment of 200 °C again to avoid the signal interference of gas pyridine (Fig. S4) and the physically adsorbed pyridine. The absorbed pyridine signal was collected by deducting the baseline as displayed in Fig. 2a. Thereinto, the bands at 1444 and 1604 cm^{-1} were ascribed to the Lewis acid sites (Ti sites), as well as no appreciable peaks were observed at 1540 cm^{-1} , which was corresponded to the Brønsted acid sites (H sites of hydroxyl) [36]. Moreover, the Lewis acid sites were susceptible to the introduction of sulfate in both $\text{TiO}_2\text{-SO}_4$ and R- $\text{TiO}_2\text{-SO}_4$ catalysts, implying the SO_4^{2-} was able to be chemically bonded with the Ti sites. Additionally, S 2p XPS spectra was adopted to gain an in-depth insight about the chemical states of SO_4 contaminated TiO_2 and R- TiO_2 in Fig. 2b. The peak at 168.6 eV of R- $\text{TiO}_2\text{-SO}_4$ which was assigned to the physisorbed SO_4^{2-} species reflected a slightly higher binding energy shift in contrast to the $\text{TiO}_2\text{-SO}_4$ catalyst [37]. Surprisingly, the band at 163.6 eV which was derived from the SO_4^{2-} species absorbed on the Ti sites in $\text{TiO}_2\text{-SO}_4$ underwent a prodigious higher-binding-energy shift towards 164.8 eV in R- $\text{TiO}_2\text{-SO}_4$. More specific peak-splitting information showed that the band located at 164.8 eV consists of deconvoluted peaks located at 163.6 eV and 164.9 eV, which can be attributed to the sulfate species adsorbed on the outer surface and hollow surfaces of the R- TiO_2 nanotube, respectively (Fig. S5). This distinct distribution exemplified that through the design of the hollow surface among R- TiO_2 , the SO_4^{2-} was coordinated with the

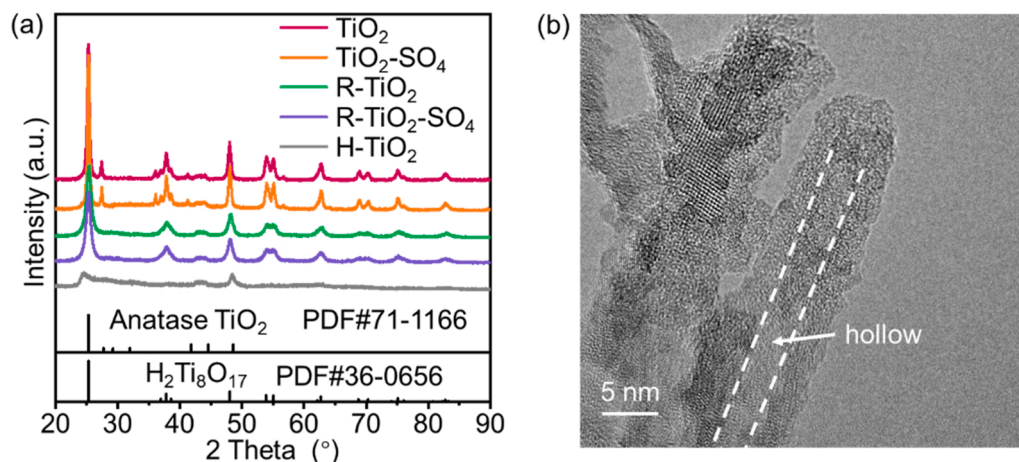


Fig. 1. (a) XRD patterns of TiO_2 , $\text{TiO}_2\text{-SO}_4$, R-TiO_2 , $\text{R-TiO}_2\text{-SO}_4$ and H-TiO_2 photocatalysts. (b) HRTEM image of R-TiO_2 photocatalysts.

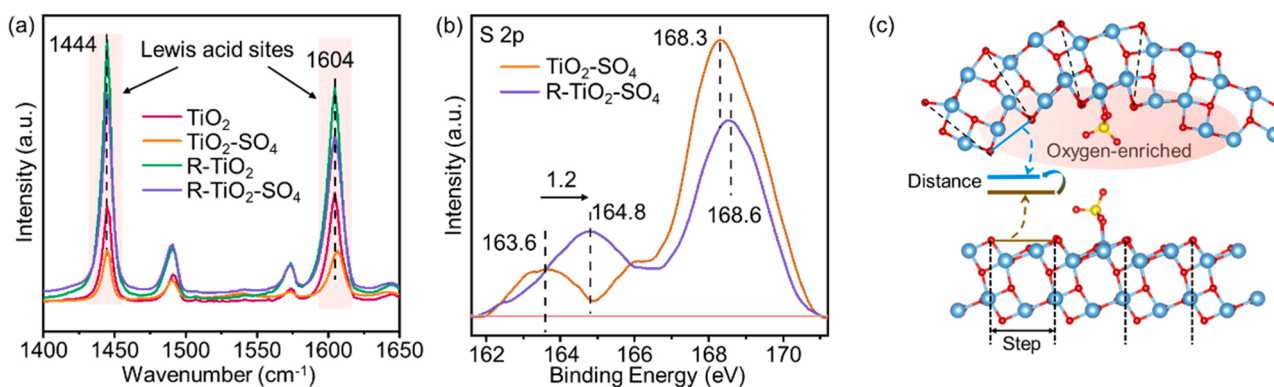


Fig. 2. (a) Adsorption spectra of pyridine-FTIR collected at 473 K for TiO_2 , $\text{TiO}_2\text{-SO}_4$, R-TiO_2 and $\text{R-TiO}_2\text{-SO}_4$ photocatalysts. (b) High resolution S 2p XPS spectra of $\text{TiO}_2\text{-SO}_4$ and $\text{R-TiO}_2\text{-SO}_4$ photocatalysts. (c) Adsorbed model of SO_4^{2-} on TiO_2 (below) and R-TiO_2 (above) photocatalysts.

Ti sites with a weak interaction in $\text{R-TiO}_2\text{-SO}_4$ while with a strong interaction in $\text{TiO}_2\text{-SO}_4$. In this regard, the electrons migrated from SO_4^{2-} to Ti site in $\text{TiO}_2\text{-SO}_4$ more dramatically (Fig. S6).

In order to further identify the sulfate distribution on $\text{R-TiO}_2\text{-SO}_4$, R-TiO_2 was first soaked in xylene before impregnated by sulfate, which allowed xylene to occupy the channels of the nanotubes. Due to the surface tension in the channels, the xylene prevented water from entering the channels, so the sulfate can only be deposited on the outer surface of the R-TiO_2 nanotubes. At this time, the S 2p XPS spectra (Fig. S7) only showed a weak peak at 168.4 eV, attributed to the high dispersion of physisorbed SO_4^{2-} species. More importantly, compared to the xylene-treated sample, the $\text{R-TiO}_2\text{-SO}_4$ showed a large proportion of the peak at 164.9 eV, proving that a large amount of sulfate entered the channels indeed. Furthermore, the Brunauer–Emmett–Teller (BET) surface area analysis (Table S1) indicated that with the sulfate adsorption on the TiO_2 surface, the surface area almost unchanged. However, the surface area of $\text{R-TiO}_2\text{-SO}_4$ ($183 \text{ m}^2/\text{g}$) suffered from a significant decline compared to R-TiO_2 ($287 \text{ m}^2/\text{g}$), further indicating the sulfate occupied the channel of the nanotubes.

Above all, the diverse SO_4^{2-} adsorption regimes were originated from the curvature modulation of Ti-O configuration among R-TiO_2 . According to the above results, the local structures of different SO_4^{2-} adsorption regime were exhibited. It was generally acknowledged that the surface of TiO_2 was constituted by the step configurations [38]. In this case, three steps were considered as a part of representative coordination geometry of TiO_2 , which can be postulated shown in Fig. 2c. Due to the effective modulation of unbent Ti-O steps among TiO_2 into bent Ti-O steps among R-TiO_2 via reconstruction process, the Ti-O steps

aggregated and the distance between the hollow-surface exposed oxygen atoms could be qualitatively regarded as decreased compared to the unbent-surface counterparts. In this case, the shorter distance between exposed oxygen atoms created an oxygen-enriched configuration in $\text{R-TiO}_2\text{-SO}_4$ catalyst and the interaction between the sulfate and the aggregated surface was moderately tuned, leading to the distinct SO_4^{2-} adsorption state in $\text{R-TiO}_2\text{-SO}_4$.

3.2. Photoelectric properties characterization

In order to investigate the effect of sulfate on photoelectric properties, UV-vis DRS spectra was first employed to investigate the light harvest ability in Fig. 3a. Obviously, no matter whether the sulfate contamination was present or not for TiO_2 and R-TiO_2 , the absorption threshold was nearly the same and no new electronic structure appeared. Concurrently, the valence band position was measured by valence-band X-ray photoelectron spectroscopy (Vb-XPS) in Fig. 3b. With a negligible variation, the valence band position can be deemed to be unchanged in all the sulfate-contaminated samples. Hence, the band structure was corroborated to be unaffected by trace sulfate both for TiO_2 and R-TiO_2 . For the impact on carrier separation, the PL spectra was recorded with emission at 475 nm in Fig. 3c. The TiO_2 showed the highest PL intensity and the curved Ti-O structure of R-TiO_2 was proved to facilitate the photogenerated carrier separation with a much attenuating signal. In addition, it should be emphasized that the different phenomenon appeared with the sulfate contamination in TiO_2 and R-TiO_2 . The sulfate inhibited the recombination of carriers on $\text{TiO}_2\text{-SO}_4$ while fostering this process on $\text{R-TiO}_2\text{-SO}_4$, which indicated that the

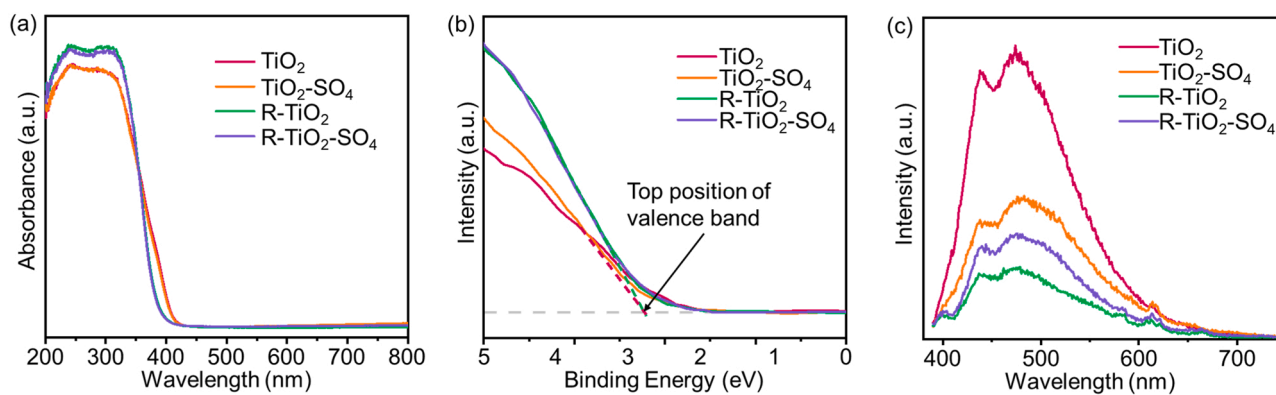


Fig. 3. (a) UV-vis DRS spectra, (b) Vb-XPS and (c) photoluminescence spectra (excitation wavelength at 375 nm) of TiO_2 , $\text{TiO}_2\text{-SO}_4$, R-TiO_2 and $\text{R-TiO}_2\text{-SO}_4$ photocatalysts.

sulfate acted as the center to attract both electrons and holes in $\text{R-TiO}_2\text{-SO}_4$, but manifested an exclusive appeal to single carrier (electrons or holes) in $\text{TiO}_2\text{-SO}_4$ [39–41].

3.3. Photocatalytic performance of benzene degradation

The performance of photocatalytic benzene degradation was conducted in a continuous flow reactor. After the concentration of components reached stable, the light was introduced and the aromatic ring was destructed into CO_2 . The corresponding concentrations were monitored by photoacoustic spectrometer analyzer in Fig. 4a and b. As the commercial photocatalyst, TiO_2 displayed a prominent performance towards benzene and an excellent mineralization ability for CO_2 [42]. Fortunately, with trace sulfate exposure, the commercial catalyst encountered a consecutive deactivation, along with the degradation rate of benzene dropping from 93.4% to 36.4% within 2 h, and the CO_2 generation was accordingly far from satisfactory as depicted. The TiO_2 samples with less sulfate deposited (0.5%, 1%) were also tested for benzene degradation (Fig. S8a), and both these samples exhibited obvious deactivation. This intriguing finding was of significance to the photocatalytic air purification, for substantial ionic substances being distributed in the actual atmosphere but rarely noticed in the previous reports. Simultaneously, the commercial photocatalyst was demonstrated to be not applied in the circumstance containing the sulfate for benzene purification. In stark contrast with TiO_2 , the R-TiO_2 yielded a prominent performance of benzene degradation and mineralization whether the sulfate was present or not. With various amount of sulfate (0.5%, 1%, 2%, 3%) contamination, the $\text{R-TiO}_2\text{-SO}_4$ still displayed an

excellent stability in long-term experiment (Fig. S8b and S9), indicating an immunity to the sulfate-induced deactivation. Meanwhile, with a sulfate deposition of 0.5 wt%, the TiO_2 (specific surface area of $66 \text{ cm}^2/\text{g}$) began to show deactivation in which the CO_2 generation was gradually decreased. As for R-TiO_2 photocatalyst (specific surface area of $287 \text{ cm}^2/\text{g}$), even with a sulfate deposition of 3 wt%, the amount of CO_2 generation had been unabated as the reaction time continued. Additionally, the ammonium and carbonate as other common ionic substances were also operated to TiO_2 and R-TiO_2 . The stable degradation rate and mineralization were confirmed that the ammonium and carbonate would not induce the deactivation (Fig. S10), further demonstrating the SO_4^{2-} was responsible for the handicaps of the sulfate.

To verify the reason of the distinct stability, Raman spectra of all samples were recorded in Fig. 5a. Wherein, all the uncontaminated samples displayed nearly equal Raman peaks before and after the degradation reaction (Fig. S11). As for the sulfate-contaminated samples, a wide band from 800 to 2000 cm^{-1} as well as the peak at 1580 cm^{-1} were observed in the reacted $\text{TiO}_2\text{-SO}_4$, which derived from the amorphous carbon and the stretching modes of sp^2 atoms in carbocycles or long chains, respectively [43,44]. These appeared signals suggested that the carbon derivatives aggregated in the function of SO_4^{2-} deposition in $\text{TiO}_2\text{-SO}_4$, and the carbon deposition was the direct reason for deactivation. For $\text{R-TiO}_2\text{-SO}_4$, the Raman signals coincided with each other before and after the reaction. It was noteworthy that the Ti-O characteristic peaks remained almost unchanged in all the samples, indicating the deactivation resulted from the surface carbonaceous species and irrelevant with the Ti-O structural change in all samples. For a more insightful deactivation information, we adopted the unreacted

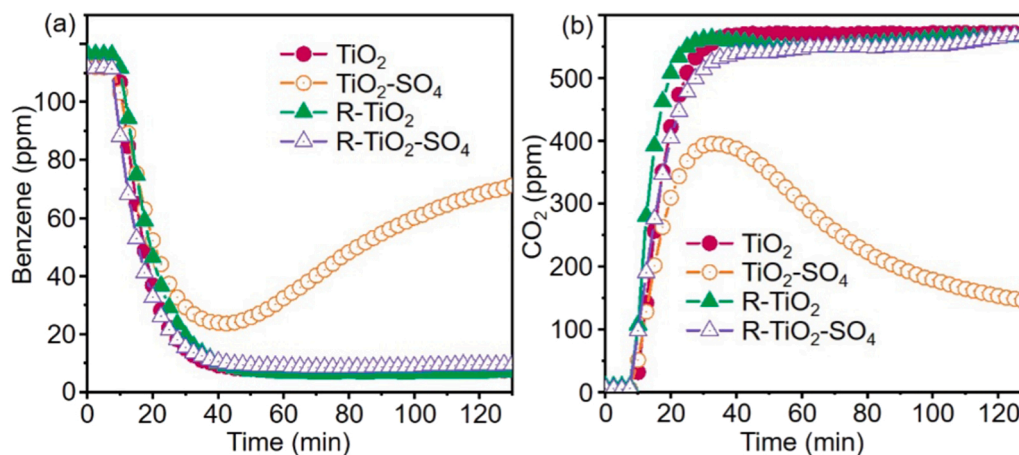


Fig. 4. Plots of concentration of (a) benzene and (b) CO_2 versus time over TiO_2 , $\text{TiO}_2\text{-SO}_4$, R-TiO_2 and $\text{R-TiO}_2\text{-SO}_4$ photocatalysts. Reaction conditions: 112 ppm of benzene, 12,000 ppm of H_2O balanced with air, $27,000 \text{ h}^{-1}$ of GHSV, and irradiated under a xenon lamp with light intensity of $0.4 \text{ W}/\text{cm}^2$.

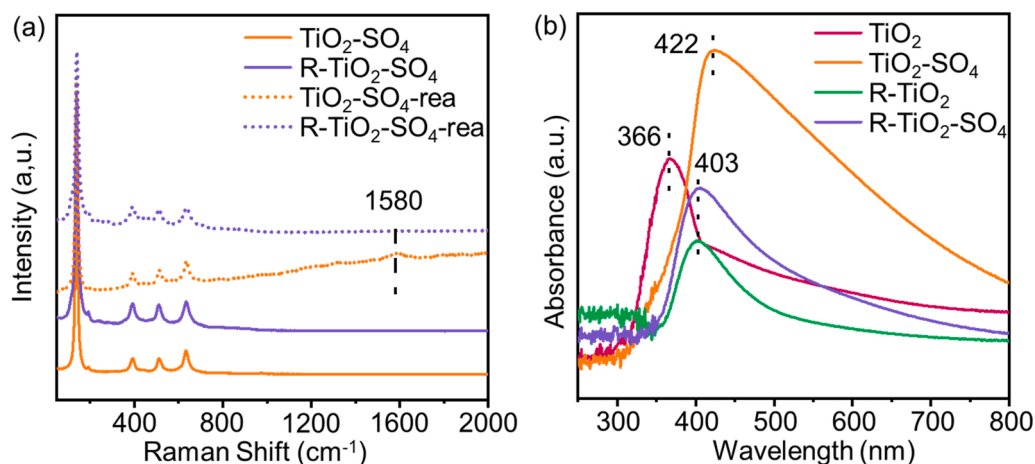


Fig. 5. (a) Raman spectra of TiO₂-SO₄ and R-TiO₂-SO₄ photocatalysts before and after the reaction. (b) UV-vis DRS spectra of the reacted TiO₂, TiO₂-SO₄, R-TiO₂ and R-TiO₂-SO₄ photocatalysts. The spectra were collected with their related unreacted sample as the reference.

photocatalysts as the baseline instead of the common BaSO₄ (Fig. S12), to collect the UV-vis DRS spectra of the reacted samples in Fig. 5b. Owing to the aforementioned information, the variable absorption threshold resulted from the carbon derivatives in the reacted samples. The peaks at 366 and 422 nm can be respectively attributed to the maleic acid in TiO₂ and benzoquinone species in TiO₂-SO₄, which will be discussed in detail for the part of *in-situ* DRIFTS. For both R-TiO₂ and R-TiO₂-SO₄ samples, the peak was located at the same position at 403 nm, which can be assigned to the phenol species. The *in-situ* UV-DRS experiments were also carried out with these samples to further identify the carbon derivatives generated during the reaction by excluding the effects of the intrinsic structure of catalysts (Fig. S13 and S14). With the gas benzene and O₂ molecule continuously absorbed, no new peaks appeared in all the samples. However, when introducing the light to trigger the reaction, the signal of intermediate species appeared, which was consistent with the results in Fig. 5b.

3.4. Deactivation and sulfate-tolerance mechanism

In order to understand the detailed pathway and the deactivation/sulfate-tolerance mechanism, the reactive oxygen species (ROS) were investigated, which was generally considered as the main active matters in photocatalytic VOCs degradation [45–47]. Thereby, radical trapping experiments were performed to detect various oxygen species. With the DMPO scavenger, the hydroxyl radicals (•OH) were quickly seized as displayed in Fig. 6a. Amazingly, extra signals appeared with the addition of sulfate, assigned to the sulfate radicals (•SO₄•, more parameters in

Table S2), which can also be trapped by DMPO [48,49]. As one of the strongest oxidative radicals, the •SO₄• was extensively applied to wastewater treatment derived from persulfate decomposition [50]. However, the sulfate radicals produced by SO₄²⁻ were rarely reported in the gas-solid interface. Due to the presence of scavenger, the recombination of photogenerated carriers was prohibited, and the EPR signal just represented the production capability of radicals. The intensity of •OH was multiplied with sulfate contamination, but the more •SO₄• and less •OH were shown in R-TiO₂-SO₄ towards TiO₂-SO₄. As was evidenced that the two catalysts delivered the similar HOMO position and bandgap in Fig. 3a and 3b, which contributed to the similar number of holes and the near total amount of oxidizing species. In this case, the phenomenon of more •SO₄• and less •OH can be understood. As for singlet oxygen (¹O₂) and superoxide radical (•O₂•) in Fig. 6b and 6c, the intensity of these radicals was notably increased with sulfate contamination and the maximum number of •O₂• and ¹O₂ were generated in R-TiO₂-SO₄, which was stem from the local enriched oxygen environment.

In order to clarify the roles of ROS in the oxidation of gas benzene, the ROS control experiments were operated by changing the atmosphere under irradiation. The benzene was degraded over the photocatalysts under different polluted atmosphere such as dry N₂ atmosphere, N₂ with 10,000 ppm H₂O, dry air, and air with 10,000 ppm H₂O. The concentration of •OH was depended on the humidity and the concentration of O₂-related ROS was controlled by the presence or absence of oxygen. As was displayed in Fig. 7a, when TiO₂ was exposed under dry N₂ atmosphere, benzene can be degraded at the beginning of the degradation

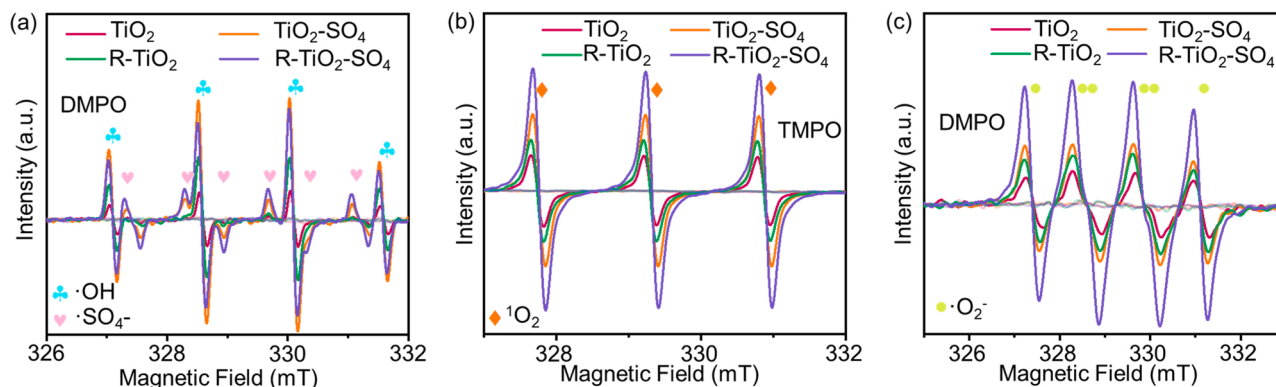


Fig. 6. *In-situ* EPR spectra before and after 10 min-light illumination over TiO₂, TiO₂-SO₄, R-TiO₂ and R-TiO₂-SO₄ photocatalysts for (a) •OH, (b) ¹O₂ and (c) •O₂• signals.

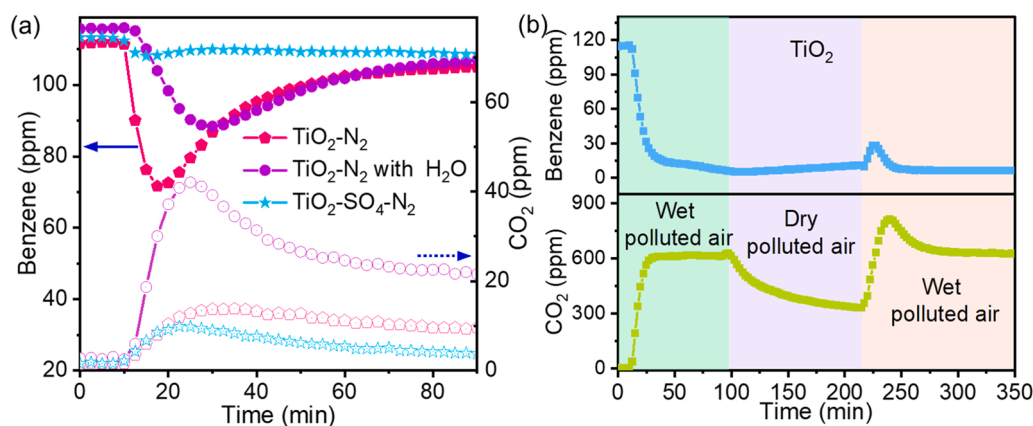


Fig. 7. Plots of benzene (solid symbol) and CO₂ (dash symbol) concentration versus time over TiO₂, TiO₂-SO₄ photocatalysts under (a) oxygen-free atmosphere and (b) atmosphere containing 21% oxygen. Reaction conditions: 112 ppm of benzene, 27,000 h⁻¹ of GHSV, and irradiated under a xenon lamp with light intensity of 0.4 W/cm².

reaction and few CO₂ can be generated, which was attributed to the absorbed ROS on the TiO₂ surface. After the absorbed ROS was depleted, the degradation of benzene was inhibited, resulting from that the carbonaceous intermediates cannot be eliminated and then accumulated on the photocatalyst surface. Notably, these intermediates which accumulated on the catalyst surface under N₂ can be eliminated by being irradiated under simulated polluted air (Fig. S15), which was totally different from the sulfate-mediated deactivation. When being irradiated under the N₂ with 10,000 ppm H₂O, TiO₂ displayed a decreased benzene degradation performance than that under dry N₂ circumstance, resulting from the competitive adsorption of H₂O molecules and benzene molecules on the catalyst. Simultaneously, the concentration of CO₂ increased remarkably, indicating that •OH was responsible for the mineralization of intermediates. In order to study the role of •SO₄, the efficiency of benzene degradation on TiO₂-SO₄ become lower than that on TiO₂ under dry N₂ atmosphere, which was due to the rapid deactivation triggered by •SO₄. Furthermore, the benzene degradation experiment was carried out in the simulated polluted air with 10,000 ppm H₂O and dry air over TiO₂ as depicted in Fig. 7b. The benzene can be efficiently mineralized into CO₂ under the oxygen-containing condition. Simultaneously, the mineralization of benzene was inhibited in dry air, which was consistent to the phenomenon observed under the conditions in dry N₂. To conclude, the O₂-related radicals were responsible for the conversion of benzene and the •OH played a significant role on the mineralization of intermediates, while the •SO₄ answered for the deactivation. Moreover, the ROS control

experiments were also carried out on the R-TiO₂ catalyst and the conclusions about the role of ROS were consistent with those on TiO₂ (Fig. S16). It was worth noting that the R-TiO₂ exhibited a much higher conversion of benzene than TiO₂ under dry N₂ atmosphere, further proving the oxygen-enrich environment in R-TiO₂.

The photocatalytic benzene degradation pathway was then explored by *in-situ* DRIFTS. After the pretreatment in air at 80 °C for 30 min, the simulated polluted air was pumped into the reaction cell and the light was introduced. The surface intermediates on TiO₂ were investigated to figure out the pathway on uncontaminated commercial catalysts, and displayed in Fig. 8a. As the reaction proceeded, the bands located at 1420–1480 cm⁻¹ and 1520–1600 cm⁻¹ were stepwise accumulated, which were assigned to the maleic acid and phenol, respectively [51–53]. Furthermore, a much weaker band within 1680–1725 cm⁻¹ attributed to the C=O stretching vibration of benzoquinone was also noticed [51,54]. The detailed information of the peaks was listed (Table S3). Based on the species monitored by *in-situ* DRIFTS, a reaction route can be concluded (Fig. S17) and followed by the benzene – phenol – benzoquinone – maleic acid – CO₂ pathway, which was also proved in other reports [55]. As for TiO₂-SO₄, the identical intermediates were noticed in Fig. 8b, but a steep accumulation of benzoquinone at 1680–1715 cm⁻¹ was becoming increasingly evident while the ratio between phenol and maleic acid species virtually unchanged. This dramatic accumulation was responsible for the deactivation occurred over TiO₂-SO₄. Besides, the intermediates on R-TiO₂ and R-TiO₂-SO₄ were recorded in Fig. 9a and b. Similar to the TiO₂ catalyst, the surface

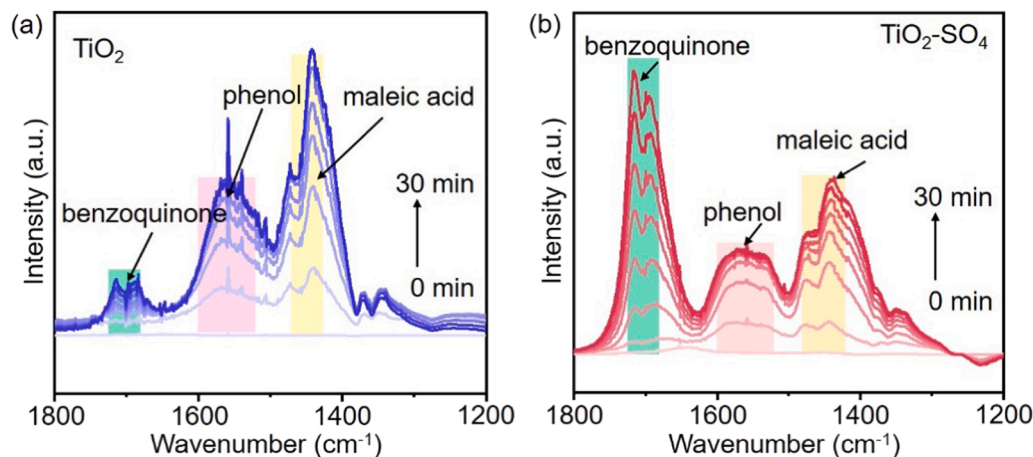


Fig. 8. *In-situ* DRIFTS of benzene degradation reaction at 300 K ranging from 1200 to 1800 cm⁻¹ over (a) TiO₂ and (b) TiO₂-SO₄ photocatalysts. Pretreatment condition: 80 °C for 30 min in air. Reaction condition: 500 ppm of benzene + 10% O₂ with wet air as balance gas and under xenon lamp light illumination.

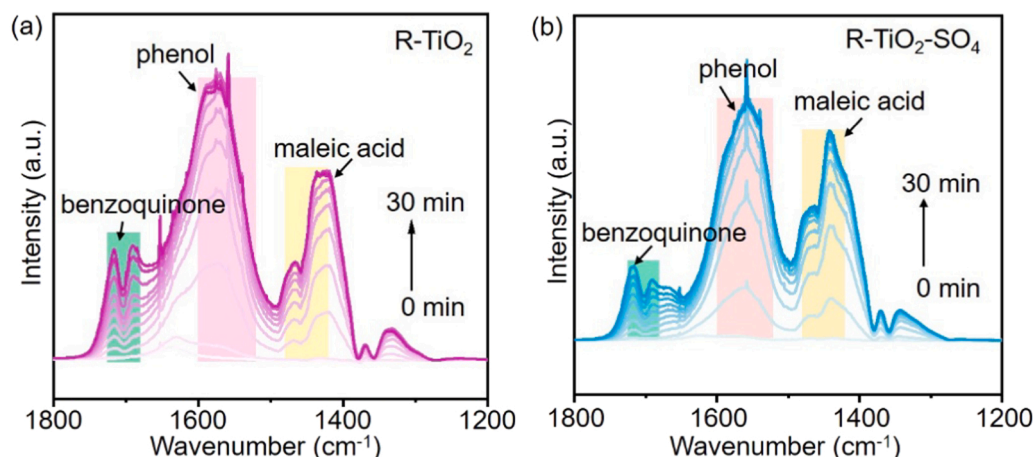


Fig. 9. In-situ DRIFTS of benzene degradation reaction at 300 K ranging from 1200 to 1800 cm^{-1} over (a) R-TiO₂ and (b) R-TiO₂-SO₄ photocatalysts. Pretreatment condition: 80 °C for 30 min in air. Reaction condition: 500 ppm of benzene + 10% O₂ with wet air as balance gas and under xenon lamp light illumination.

species on R-TiO₂ and R-TiO₂-SO₄ were assigned to phenol, benzoquinone and maleic acid. Moreover, the band intensity of benzoquinone remained at a low level even with the sulfate contamination in R-TiO₂-SO₄.

Thereby, the accumulation of benzoquinone answered for the deactivation of the commercial TiO₂ catalyst. Based on all the conclusions, the deactivation mechanism of TiO₂ and corresponding immune mechanism of R-TiO₂ were put forward in Fig. 10. The adsorbed SO₄²⁻ was evolved into •SO₄ under the irradiation, which sequentially reacted with the benzene. By the deoxygenation of •SO₄, benzene was quickly converted into benzoquinone and the •SO₄ transformed into •SO₃. However, the sulfate on the TiO₂ surface preferred to trap holes based on the enhanced carrier separation capability in Fig. 3c, leading to the fact that the •SO₃ species cannot be annihilated. Simultaneously, due to the unbent steps in TiO₂, the steric ROS spread in all directions and cannot be gathered, which was unable to effectively supplement oxygen for •SO₃ to restore SO₄²⁻. In these contributions, the •SO₃ intimately coupled with benzoquinone and formed the low-lying stable intermediate. As the reaction proceeded, the •SO₃ continued to deoxygenate and fixed more benzoquinone species accompanying with the benzoquinones further polymerized between each other. Thereby, the molecule building blocks

of benzoquinone eventually encountered the block of active sites and led to the deactivation. By a tactful design of the curvature modulation among R-TiO₂, the bent-state steps aggregated the oxygen and created an oxygen-enriched environment. In this regard, the subsequently generated ROS can immediately bond with •SO₃ and the benzoquinone can detach from the sulfate to the sequential reaction, realizing the self-adaptive deoxygenation of •SO₄ and the immune for the sulfate-mediate deactivation.

4. Conclusions

Photocatalytic oxidation technique is considered as an environmentally benign scenario for volatile organic compounds purification. Tremendous efforts are involved under ideal reaction conditions to effectively degrade the volatile organic compounds while the complex interactions between various air pollutant components are always ignored. As a common ionic substance component in atmosphere, trace sulfate on the surface of commercial TiO₂ will encounter rapid deactivation in photocatalytic benzene degradation. The sulfate-related radicals will promote the polymerization of benzoquinone and lead to coverage of active sites under irradiation. By means of reaction kinetic

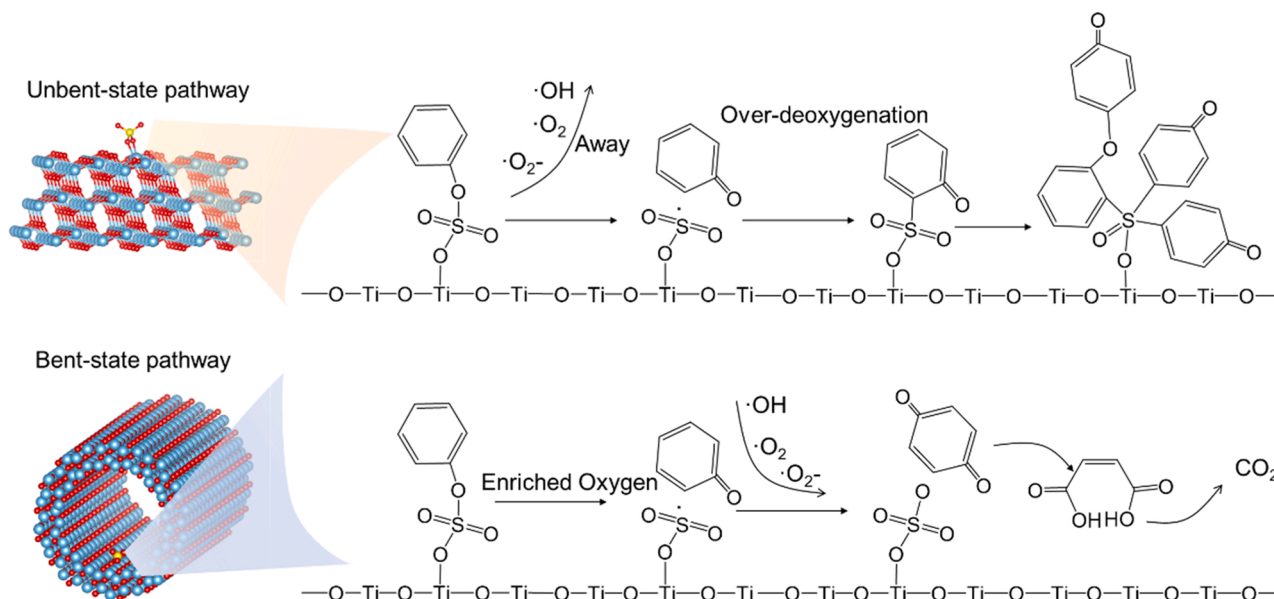


Fig. 10. Schematic illustration of unbent-state and bent-state benzene degradation pathway.

design, we successfully tailored the Ti-O steps configuration of TiO₂ from an unbent state to bent state and the modulated photocatalyst realized the resistance to this sulfate-mediate deactivation by self-adaptive deoxygenation of $\bullet\text{SO}_4^-$. This work elucidates the mutative reaction pathway induced by atmospheric ionic substances in photocatalytic benzene degradation and provide a strategy for developing efficient and stable photocatalysts in the actual reaction condition for efficient volatile organic compounds purification.

CRedit authorship contribution statement

Wenqiang Qu: Investigation, Data curation, Formal analysis, Writing – original draft. **Penglu Wang:** Methodology, Investigation, Formal analysis, Writing – review & editing. **Xin Chen:** Methodology, Investigation. **Dengsong Zhang:** Conceptualization, Investigation, Validation, Methodology, Resources, Writing – review & editing, Funding acquisition.

Declaration of Competing Interest

The authors declare that they have no known competing financial interests or personal relationships that could have appeared to influence the work reported in this paper.

Data Availability

Data will be made available on request.

Acknowledgments

We acknowledge the support of the National Natural Science Foundation of China (22125604).

Appendix A. Supporting information

Supplementary data associated with this article can be found in the online version at [doi:10.1016/j.apcatb.2022.122036](https://doi.org/10.1016/j.apcatb.2022.122036).

References

- [1] D. Wu, H. Zheng, Q. Li, L. Jin, R. Lyu, X. Ding, Y. Huo, B. Zhao, J. Jiang, J. Chen, X. Li, S. Wang, Toxic potency-adjusted control of air pollution for solid fuel combustion, *Nat. Energy* 7 (2022) 194–202, <https://doi.org/10.1038/s41560-021-00951-1>.
- [2] S. Hattori, Y. Iizuka, B. Alexander, S. Ishino, K. Fujita, S. Zhai, T. Sherwen, N. Oshima, R. Uemura, A. Yamada, N. Suzuki, S. Matoba, A. Tsuruta, J. Savarino, N. Yoshida, Isotopic evidence for acidity-driven enhancement of sulfate formation after SO₂ emission control, *Sci. Adv.* 7 (2021) eabd4610, <https://doi.org/10.1126/sciadv.abd4610>.
- [3] B. Gu, L. Zhang, R. Van Dingenen, M. Vieno, J.M. Van Grinsven, X. Zhang, S. Zhang, Y. Chen, S. Wang, C. Ren, S. Rao, M. Holland, W. Winiwarter, D. Chen, J. Xu, A. Sutton Mark, Abating ammonia is more cost-effective than nitrogen oxides for mitigating PM_{2.5} air pollution, *Science* 374 (2021) 758–762, <https://doi.org/10.1126/science.abf8623>.
- [4] X. Mei, X. Zhu, Y. Zhang, Z. Zhang, Z. Zhong, Y. Xin, J. Zhang, Decreasing the catalytic ignition temperature of diesel soot using electrified conductive oxide catalysts, *Nat. Catal.* 4 (2021) 1002–1011, <https://doi.org/10.1038/s41929-021-00702-1>.
- [5] Z. Si, Y. Shen, J. He, T. Yan, J. Zhang, J. Deng, D. Zhang, SO₂-induced alkali resistance of FeVO₄/TiO₂ catalysts for NO_x reduction, *Environ. Sci. Technol.* 56 (2022) 605–613, <https://doi.org/10.1021/acs.est.1c05686>.
- [6] I. Song, H. Lee, S.W. Jeon, I.A.M. Ibrahim, J. Kim, Y. Byun, D.J. Koh, J.W. Han, D. H. Kim, Simple physical mixing of zeolite prevents sulfur deactivation of vanadia catalysts for NO_x removal, *Nat. Commun.* 12 (2021) 901, <https://doi.org/10.1038/s41467-021-21228-x>.
- [7] O. Debono, V. Hequet, L. Le Coq, N. Locoge, F. Thevenet, VOC ternary mixture effect on ppb level photocatalytic oxidation: Removal kinetic, reaction intermediates and mineralization, *Appl. Catal., B* 218 (2017) 359–369, <https://doi.org/10.1016/j.apcatb.2017.06.070>.
- [8] P. Zhang, P. Wang, A. Chen, L. Han, T. Yan, J. Zhang, D. Zhang, Alkali-resistant catalytic reduction of NO_x by using Ce–O–B alkali-capture sites, *Environ. Sci. Technol.* 55 (2021) 11970–11978, <https://doi.org/10.1021/acs.est.1c02882>.
- [9] A. Mahmood, G. Shi, Z. Wang, Z. Rao, W. Xiao, X. Xie, J. Sun, Carbon quantum dots-TiO₂ nanocomposite as an efficient photocatalyst for the photodegradation of aromatic ring-containing mixed VOCs: An experimental and DFT studies of adsorption and electronic structure of the interface, *J. Hazard. Mater.* 401 (2021) 123402, <https://doi.org/10.1016/j.jhazmat.2020.123402>.
- [10] P. Khare, J. Machesky, R. Soto, M. He, A.A. Presto, D.R. Gentner, Asphalt-related emissions are a major missing nontraditional source of secondary organic aerosol precursors, *Sci. Adv.* 6 (2020) eabb9785, <https://doi.org/10.1126/sciadv.abb9785>.
- [11] J. Meng, X. Wang, X. Yang, A. Hu, Y. Guo, Y. Yang, Enhanced gas-phase photocatalytic removal of aromatics over direct Z-scheme-dictated H₃PW₁₂O₄₀/g-C₃N₄ film-coated optical fibers, *Appl. Catal. B* 251 (2019) 168–180, <https://doi.org/10.1016/j.apcatb.2019.03.063>.
- [12] Y. Ji, Q. Shi, Y. Li, T. An, J. Zheng, J. Peng, Y. Gao, J. Chen, G. Li, Y. Wang, F. Zhang, A.L. Zhang, J. Zhao, M.J. Molina, R. Zhang, Carbenium ion-mediated oligomerization of methylglyoxal for secondary organic aerosol formation, *Proc. Natl. Acad. Sci. U. S. A.* 117 (2020) 13294–13299, <https://doi.org/10.1073/pnas.1912235117>.
- [13] C. McDonald Brian, A. de Gouw Joost, B. Gilman Jessica, H. Jathar Shantanu, A. Akherati, D. Cappa Christopher, L. Jimenez Jose, J. Lee-Taylor, L. Hayes Patrick, A. McKeen Stuart, Y. Cui Yu, S.-W. Kim, R. Gentner Drew, G. Isaacman-VanWertz, H. Goldstein Allen, A. Harley Robert, J. Frost Gregory, M. Roberts James, B. Ryerson Thomas, M. Trainer, Volatile chemical products emerging as largest petrochemical source of urban organic emissions, *Science* 359 (2018) 760–764, <https://doi.org/10.1126/science.aag0524>.
- [14] W. Qu, P. Wang, M. Gao, J.-y Hasegawa, Z. Shen, Q. Wang, R. Li, D. Zhang, Delocalization effect promoted the indoor air purification via directly unlocking the ring-opening pathway of toluene, *Environ. Sci. Technol.* 54 (2020) 9693–9701, <https://doi.org/10.1021/acs.est.0c02906>.
- [15] J. Liu, P. Wang, W. Qu, H. Li, L. Shi, D. Zhang, Nanodiamond-decorated ZnO catalysts with enhanced photocorrosion-resistance for photocatalytic degradation of gaseous toluene, *Appl. Catal. B* 257 (2019), 117880, <https://doi.org/10.1016/j.apcatb.2019.117880>.
- [16] X. Qian, D. Yue, Z. Tian, M. Reng, Y. Zhu, M. Kan, T. Zhang, Y. Zhao, Carbon quantum dots decorated Bi₂WO₆ nanocomposite with enhanced photocatalytic oxidation activity for VOCs, *Appl. Catal., B* 193 (2016) 16–21, <https://doi.org/10.1016/j.apcatb.2016.04.009>.
- [17] R. Chen, J. Li, X. Li, J. Wang, T. Huang, W. Liu, F. Dong, Unraveling the unique role of methyl position on the ring-opening barrier in photocatalytic decomposition of xylene isomers, *ACS Catal.* 12 (2022) 8363–8371, <https://doi.org/10.1021/acscatal.2c01418>.
- [18] L. Yan, Q. Wang, W. Qu, T. Yan, H. Li, P. Wang, D. Zhang, Tuning Ti³⁺-V_o-Pt⁶⁺ interfaces over Pt/TiO₂ catalysts for efficient photocatalytic oxidation of toluene, *Chem. Eng. J.* 431 (2022), 134209, <https://doi.org/10.1016/j.cej.2021.134209>.
- [19] M. Stucchi, F. Galli, C.L. Bianchi, C. Pirola, D.C. Boffito, F. Biasoli, V. Capucci, Simultaneous photodegradation of VOC mixture by TiO₂ powders, *Chemosphere* 193 (2018) 198–206, <https://doi.org/10.1016/j.chemosphere.2017.11.003>.
- [20] Xa Dong, Z. Cui, Y. Sun, F. Dong, Humidity-independent photocatalytic toluene mineralization benefits from the utilization of edge hydroxyls in layered double hydroxides (LDHs): a combined operando and theoretical investigation, *ACS Catal.* 11 (2021) 8132–8139, <https://doi.org/10.1021/acscatal.1c01599>.
- [21] K. Li, H. Wang, L. Chen, J. Li, F. Dong, Synergistic degradation of NO and C₇H₈ for inhibition of O₃ generation, *Appl. Catal., B* 312 (2022), 121423, <https://doi.org/10.1016/j.apcatb.2022.121423>.
- [22] F. He, W. Jeon, W. Choi, Photocatalytic air purification mimicking the self-cleaning process of the atmosphere, *Nat. Commun.* 12 (2021) 2528, <https://doi.org/10.1038/s41467-021-22839-0>.
- [23] S. Weon, F. He, W. Choi, Status and challenges in photocatalytic nanotechnology for cleaning air polluted with volatile organic compounds: visible light utilization and catalyst deactivation, *Environ. Sci. Nano* 6 (2019) 3185–3214, <https://doi.org/10.1039/C9EN00891H>.
- [24] J. Li, R. Chen, W. Cui, Xa Dong, H. Wang, K.-H. Kim, Y. Chu, J. Sheng, Y. Sun, F. Dong, Synergistic photocatalytic decomposition of a volatile organic compound mixture: high efficiency, reaction mechanism, and long-term stability, *ACS Catal.* 10 (2020) 7230–7239, <https://doi.org/10.1021/acscatal.0c00693>.
- [25] J. Chen, J. Yi, W. Zhu, W. Zhang, T. An, Oxygen isotope tracing study to directly reveal the role of O₂ and H₂O in the photocatalytic oxidation mechanism of gaseous monoaromatics, *Environ. Sci. Technol.* 55 (2021) 16617–16626, <https://doi.org/10.1021/acs.est.1c05134>.
- [26] Z. Xu, W. Chai, J. Cao, F. Huang, T. Tong, S. Dong, Q. Qiao, L. Shi, H. Li, X. Qian, Z. Bian, Controlling the gas–water interface to enhance photocatalytic degradation of volatile organic compounds, *ACS EST Eng.* 1 (2021) 1140–1148, <https://doi.org/10.1021/acsestengg.1c00120>.
- [27] Y. Zhao, M. Xi, Q. Zhang, Z. Dong, M. Ma, K. Zhou, W. Xu, J. Xing, B. Zheng, Z. Wen, X. Liu, C.P. Nielsen, Y. Liu, Y. Pan, L. Zhang, Decline in bulk deposition of air pollutants in China lags behind reductions in emissions, *Nat. Geosci.* 15 (2022) 190–195, <https://doi.org/10.1038/s41561-022-00899-1>.
- [28] E. Dovrou, H. Bates Kelvin, M. Moch Jonathan, J. Mickley Loretta, J. Jacob Daniel, N. Keutsch Frank, Catalytic role of formaldehyde in particulate matter formation, *Proc. Natl. Acad. Sci. U. S. A.* 119 (2022), e2113265119, <https://doi.org/10.1073/pnas.2113265119>.
- [29] V. Héquet, C. Raillard, O. Debono, F. Thévenet, N. Locoge, L. Le Coq, Photocatalytic oxidation of VOCs at ppb level using a closed-loop reactor: The mixture effect, *Appl. Catal. B* 226 (2018) 473–486, <https://doi.org/10.1016/j.apcatb.2017.12.041>.
- [30] C. Zhang, J. Zhang, Y. Shen, J. He, W. Qu, J. Deng, L. Han, A. Chen, D. Zhang, Synergistic catalytic elimination of NO_x and chlorinated organics: cooperation of

- acid sites, *Environ. Sci. Technol.* 56 (2022) 3719–3728, <https://doi.org/10.1021/acs.est.1c08009>.
- [31] R. Han, R. Andrews, C. O'Rourke, S. Hodgen, A. Mills, Photocatalytic air purification: effect of HNO₃ accumulation on NO_x and VOC removal, *Catal. Today* 380 (2021) 105–113, <https://doi.org/10.1016/j.cattod.2021.04.017>.
- [32] J. Zhang, K. Vikrant, K.-H. Kim, F. Dong, M. Won Chung, S. Weon, Unveiling the collective effects of moisture and oxygen on the photocatalytic degradation of m-Xylene using a titanium dioxide supported platinum catalyst, *Chem. Eng. J.* 439 (2022), 135747, <https://doi.org/10.1016/j.cej.2022.135747>.
- [33] R. Chen, J. Li, H. Wang, P. Chen, Xa Dong, Y. Sun, Y. Zhou, F. Dong, Photocatalytic reaction mechanisms at a gas–solid interface for typical air pollutant decomposition, *J. Mater. Chem. A* 9 (2021) 20184–20210, <https://doi.org/10.1039/D1TA03705F>.
- [34] P. Wang, S. Chen, S. Gao, J. Zhang, H. Wang, Z. Wu, Niobium oxide confined by ceria nanotubes as a novel SCR catalyst with excellent resistance to potassium, phosphorus, and lead, *Appl. Catal. B* 231 (2018) 299–309, <https://doi.org/10.1016/j.apcatb.2018.03.024>.
- [35] X. Chen, P. Wang, P. Fang, T. Ren, Y. Liu, C. Cen, H. Wang, Z. Wu, Tuning the property of Mn-Ce composite oxides by titanate nanotubes to improve the activity, selectivity and SO₂/H₂O tolerance in middle temperature NH₃-SCR reaction, *Fuel Process. Technol.* 167 (2017) 221–228, <https://doi.org/10.1016/j.fuproc.2017.07.018>.
- [36] G. Zhou, F. Wang, R. Shi, Nanoparticulate Ru on morphology-manipulated and Ti³⁺ defect-riched TiO₂ nanosheets for benzene semi-hydrogenation, *J. Catal.* 398 (2021) 148–160, <https://doi.org/10.1016/j.jcat.2021.04.017>.
- [37] H. Qiu, S. Zhang, B. Pan, W. Zhang, L. Lv, Effect of sulfate on Cu(II) sorption to polymer-supported nano-iron oxides: behavior and XPS study, *J. Colloid Interface Sci.* 366 (2012) 37–43, <https://doi.org/10.1016/j.jcis.2011.09.070>.
- [38] W. Yuan, B. Zhu, K. Fang, X.-Y. Li, T.W. Hansen, Y. Ou, H. Yang, J.B. Wagner, Y. Gao, Y. Wang, Z. Zhang, In situ manipulation of the active Au-TiO₂ interface with atomic precision during CO oxidation, *Science* 371 (2021) 517–521, <https://doi.org/10.1126/science.abe3558>.
- [39] Z. Yang, Y. Shi, H. Li, C. Mao, X. Wang, X. Liu, X. Liu, L. Zhang, Oxygen and chlorine dual vacancies enable photocatalytic O₂ dissociation into monatomic reactive oxygen on BiOCl for refractory aromatic pollutant removal, *Environ. Sci. Technol.* 56 (2022) 3587–3595, <https://doi.org/10.1021/acs.est.1c08532>.
- [40] R. Qi, P. Yu, J. Zhang, W. Guo, Y. He, H. Hojo, H. Einaga, Q. Zhang, X. Liu, Z. Jiang, W. Shangguan, Efficient visible light photocatalysis enabled by the interaction between dual cooperative defect sites, *Appl. Catal. B* 274 (2020), 119099, <https://doi.org/10.1016/j.apcatb.2020.119099>.
- [41] M. Yousefi, S. Villar-Rodil, J.I. Paredes, A.Z. Moshfegh, Oxidized graphitic carbon nitride nanosheets as an effective adsorbent for organic dyes and tetracycline for water remediation, *J. Alloy. Compd.* 809 (2019), 151783, <https://doi.org/10.1016/j.jallcom.2019.151783>.
- [42] Z. Chen, Y. Peng, J. Chen, C. Wang, H. Yin, H. Wang, C. You, J. Li, Performance and mechanism of photocatalytic toluene degradation and catalyst regeneration by thermal/UV treatment, *Environ. Sci. Technol.* 54 (2020) 14465–14473, <https://doi.org/10.1021/acs.est.0c06048>.
- [43] E. Picheau, A. Impellizzeri, D. Rybkovskiy, M. Bayle, J.-Y. Mevellec, F. Hof, H. Saadaoui, L. Noé, A.C. Torres Dias, J.-L. Duval, M. Monthieux, B. Humbert, P. Puech, C.P. Ewels, A. Pénicaud, Intense raman D band without disorder in flattened carbon nanotubes, *ACS Nano* 15 (2021) 596–603, <https://doi.org/10.1021/acsnano.0c06048>.
- [44] M.S. Dresselhaus, A. Jorio, M. Hofmann, G. Dresselhaus, R. Saito, Perspectives on carbon nanotubes and graphene Raman spectroscopy, *Nano Lett.* 10 (2010) 751–758, <https://doi.org/10.1021/nl904286r>.
- [45] F. Zhang, X. Li, Q. Zhao, G. Chen, Q. Zhang, High-performance In₂O₃@PANI core@shell architectures with ultralong charge carriers lifetime for photocatalytic degradation of gaseous 1,2-dichlorobenzene, *Appl. Catal. B* 263 (2020), 118278, <https://doi.org/10.1016/j.apcatb.2019.118278>.
- [46] F. He, S. Weon, W. Jeon, M.W. Chung, W. Choi, Self-wetting triphase photocatalysis for effective and selective removal of hydrophilic volatile organic compounds in air, *Nat. Commun.* 12 (2021) 6259, <https://doi.org/10.1038/s41467-021-26541-z>.
- [47] A. Talaiekhozani, S. Rezaei, K.-H. Kim, R. Sanaye, A.M. Amani, Recent advances in photocatalytic removal of organic and inorganic pollutants in air, *J. Clean. Prod.* 278 (2021), 123895, <https://doi.org/10.1016/j.jclepro.2020.123895>.
- [48] X. Xie, R. Xie, Z. Suo, H. Huang, M. Xing, D. Lei, A highly dispersed Co-Fe bimetallic catalyst to activate peroxymonosulfate for VOC degradation in a wet scrubber, *Environ. Sci. Nano* 8 (2021) 2976–2987, <https://doi.org/10.1039/D1EN00547B>.
- [49] Y. Yang, G. Banerjee, G.W. Brudvig, J.-H. Kim, J.J. Pignatello, Oxidation of organic compounds in water by unactivated peroxymonosulfate, *Environ. Sci. Technol.* 52 (2018) 5911–5919, <https://doi.org/10.1021/acs.est.8b00735>.
- [50] C. Dong, Y. Bao, T. Sheng, Q. Yi, Q. Zhu, B. Shen, M. Xing, I.M.C. Lo, J. Zhang, Singlet oxygen triggered by robust bimetallic MoFe/TiO₂ nanospheres of highly efficacy in solar-light-driven peroxymonosulfate activation for organic pollutants removal, *Appl. Catal. B* 286 (2021), 119930, <https://doi.org/10.1016/j.apcatb.2021.119930>.
- [51] Y. Guo, D.-P. Yang, M. Liu, X. Zhang, Y. Chen, J. Huang, Q. Li, R. Luque, Enhanced catalytic benzene oxidation over a novel waste-derived Ag/eggshell catalyst, *J. Mater. Chem. A* 7 (2019) 8832–8844, <https://doi.org/10.1039/C8TA10822F>.
- [52] Y. Liang, Y. Liu, J. Deng, K. Zhang, Z. Hou, X. Zhao, X. Zhang, K. Zhang, R. Wei, H. Dai, Coupled palladium–tungsten bimetallic nanosheets/TiO₂ hybrids with enhanced catalytic activity and stability for the oxidative removal of benzene, *Environ. Sci. Technol.* 53 (2019) 5926–5935, <https://doi.org/10.1021/acs.est.9b00370>.
- [53] Z. Hou, L. Dai, Y. Liu, J. Deng, L. Jing, W. Pei, R. Gao, Y. Feng, H. Dai, Highly efficient and enhanced sulfur resistance supported bimetallic single-atom palladium–cobalt catalysts for benzene oxidation, *Appl. Catal. B* 285 (2021), 119844, <https://doi.org/10.1016/j.apcatb.2020.119844>.
- [54] X. Liu, Y. Zhang, S. Matsushima, H. Hojo, H. Einaga, Photocatalytic oxidation process for treatment of gas phase benzene using Ti³⁺ self-doped TiO₂ microsphere with sea urchin-like structure, *Chem. Eng. J.* 402 (2020), 126220, <https://doi.org/10.1016/j.cej.2020.126220>.
- [55] H. Zhuang, Q. Gu, J. Long, H. Lin, H. Lin, X. Wang, Visible light-driven decomposition of gaseous benzene on robust Sn²⁺-doped anatase TiO₂ nanoparticles, *RSC Adv.* 4 (2014) 34315–34324, <https://doi.org/10.1039/C4RA05904B>.